Title

Relaxation Time Measurement: Correlating Diffraction Patterns

Mini-abstract

This study compares one-time and two-time correlation functions for analyzing temporal changes in diffraction patterns. It finds that two-time correlation functions require shorter observation times and show small sensitivity to radiation dose, highlighting the advantage of two-time correlation functions in assessing dynamics in liquids and glasses via electron diffraction.

Abstract

Dynamics in liquids and glasses can be assessed using X-ray photon correlation spectroscopy or electron correlation microscopy, which involves measuring the temporal changes in diffraction patterns. Two methods are commonly used to evaluate these temporal changes: one-time correlation function or two-time correlation function. However, the specific characteristics of these methods have not been thoroughly studied. In this study, we investigated the differences between these methods and found that the two-time correlation function can measure dynamics for longer periods than the method relying on the one-time correlation function. Additionally, we demonstrated that the two-time correlation function exhibits a weak

dependence on the amount of dose applied.

Introduction

X-ray Photon Correlation Spectroscopy (XPCS) and Electron Correlation Microscopy (ECM) have been utilized to assess the dynamics of atoms or particles in non-crystalline materials such as liquids and glasses [1,2]. These techniques gauge dynamics through temporal diffraction patterns. In these patterns, high-intensity spots, referred to as speckles, appear when the atomic structures exhibit local orders like short-range or medium-range order [3]. Additionally, the well-known diffraction pattern of glasses, known as the halo pattern, is formed by accumulating speckles from numerous local structures when X-rays or electron beams irradiate a wide area. This relationship is similar to how the diffraction pattern of polycrystalline materials forms Debye-Scherrer rings. Since speckles reflect the local atomic structure of the material, fluctuations in speckle intensity indicate changes in the local atomic structure. In XPCS and ECM, dynamics are gauged from the autocorrelation of intensity fluctuation and assessed by the relaxation time, which indicates the time for correlation attenuation; longer relaxation times signify slower dynamics and vice versa. In other words, these methods evaluate atomic motion in the amorphous atomic structure through the changes in the speckle pattern that arise from variations in the atomic structures.

Since an electron beam can converge down to sub-nm scales, unlike XPCS, ECM can measure

local dynamics[4]. However, this measurement is confined to a fixed point, making it challenging to measure the spatial distribution of relaxation time. Tilted Dark Field (tDF) microscopy has overcome this limitation, enabling the measurement of spatial distributions of relaxation time at the nanoscale[5]. This method uses a portion of the diffraction pattern to generate real-space dark-field images and measures the relaxation time through the temporal change of intensities at each pixel in the real-space image. Furthermore, the five-dimensional scanning transmission electron microscopy (5D-STEM) method has recently been proposed and applied to measure the spatial distribution of relaxation times [6–8]. 5D-STEM captures the spatiotemporal distribution of diffraction patterns, allowing the measurement of relaxation times from time-series diffraction patterns at each scanning point. Compared to tDF, which sacrifices the acquisition of the diffraction pattern itself to obtain the spatial distribution of relaxation times, 5D-STEM acquires the whole spatiotemporal distribution of diffraction patterns. This difference enables 5D-STEM to simultaneously analyze structure and relaxation time, making it distinct in the method of measuring relaxation time. In this paper, we investigate the differences in methods for measuring relaxation times.

Two types of relaxation time measurement methods are applicable to a 5D-STEM data set: one measures relaxation time from intensity modulation, similar to XCPS, ECM, and tDF [4,9], while the other obtains relaxation time from the correlation of diffraction patterns, as demonstrated by Nakazawa et al. [6,8]. The former is called one-time correlation function (OTCF),

and the latter is called two-time correlation function (TTCF). The differences between these measuring methods have not been thoroughly investigated. Additionally, while the influence of electron beam irradiation on the OTCF method has been studied [10,11], it has not been explored for the TTCF method. In this study, we examine the differences between the OTCF and TTCF methods by comparing the relaxation time measurement results derived from the same 5D-STEM data set. We also present the influence of electron dose on the correlation-based method.

Methods

In this experiment, we selected $Zr_{50}Cu_{40}Al_{10}$ metallic glass as the sample (purchased from DIAVAC Ltd.). The TEM sample was prepared using the Focused Ion Beam (JEOL JIB-4000). The sample was heated to 653 K using the Fusion heating holder (Protochips Inc.). 5D-STEM observation was performed using the JEM-ARM200F (JEOL Ltd.) and 4DCanvas (JEOL Ltd.) with an acceleration voltage of 200 kV, a convergence semi-angle of 1.6 mrad, 60×180 scan points, and a scan step of 0.27 nm. The diameter of the electron beam in real space was 0.78 nm (full width at half maximum) with this setting. The dwell time was 133 μs, and the number of pixels in the diffraction pattern was 264×66 pixels (hardware binned by 4 along the k_y direction). The total number of measured diffraction patterns was 8388608, and the observation time was 1115.6 s. A beam stopper was used to prevent blooming caused by the transmitted beam. Following the measurements, we binned the diffraction pattern by 4 along the k_x

77 direction to correct the aspect ratio. Consequently, the number of pixels in the diffraction
78 pattern and the pixel size became 66×66 and 0.23 nm^{-1}, respectively. Approximately 600
79 diffraction patterns were obtained at each scanning point. We conducted this measurement
80 using three different dose amounts: 11.5 pA, 5.8 pA, and 2.8 pA. The sample thickness
81 measured by EELS was approximately 50 nm (See supplemental Fig. S1) and does not
82 significantly affect the measurement of the relaxation time (See supplemental Fig. S2). To
83 avoid abrupt changes in relaxation time by aging during the 5D-STEM measurement, we
84 started measurements 3 hours after heating[12]. In supplemental, we discussed the effect of spatial
85 resolution in real space and angular resolution in diffraction (supplemental Fig. S3) and showed
86 the obtained diffraction pattern under 11.5 pA electron dose (supplemental Fig. S4).
87
88 **Results and Discussions**
89 **Difference between one-time correlation function and two-time correlation function**
90 In this section, we delineate the disparity between the OTCF and TTCF methods. Both
91 methods gauge relaxation time through time-series diffraction patterns using two steps: 1)
92 measuring temporal decay due to atomic displacements and 2) fitting a decay function such as
93 the Kohlrausch-Williams-Watts (KWW) function $f(t) = \exp\left(-2\left(\frac{t}{\tau}\right)^{\gamma}\right)$ to ascertain
94 relaxation time τ. γ is a fitting parameter known as the stretching exponent, and t is time.
95 The distinction between the OTCF and TTCF solely arises in step 1, with no variation in step

2. It is important to note that neither method directly gauges dynamics from atomic displacements. Here, we elucidate the contrast between these approaches. The schematics of both methods are depicted in Figure 1. The OTCF estimates dynamics through the temporal change of intensity, while the TTCF estimates dynamics through changes in the correlation of temporal diffraction patterns. Using reciprocal vertical and horizontal positions defined as $\boldsymbol{k} = (k_x,\ k_y)$ and time as t, the intensity of a diffraction pattern at $\boldsymbol{k}$ and t is denoted as $I(\boldsymbol{k}, t)$. Time-series diffraction patterns are recorded with a fixed interval time Δt. The OTCF calculates the autocorrelation of intensity fluctuations $g_{one}(\boldsymbol{k}, t)$ at a specific position $\boldsymbol{k}$ in the diffraction pattern[5] by the following equation.

[Figure 1 here]

$$g_{one}(\boldsymbol{k}, j\Delta t) = \frac{(N-j)\sum_{i=1}^{N-j} I(\boldsymbol{k}, t_i) I\left(\boldsymbol{k}, t_{i+j}\right)}{\left[\sum_{i=1}^{N-j} I(\boldsymbol{k}, t_i)\right]\left[\sum_{i=1}^{N-j} I\left(\boldsymbol{k}, t_{i+j}\right)\right]}. \quad (1)$$

N denotes the total number of diffraction patterns in time series, i and j are the natural numbers and represent the index of the series. Then, t_i denote the time at which the i-th diffraction pattern was acquired. In tDF, $\boldsymbol{k}$ is determined by the position of the objective aperture. Meanwhile, XPCS and ECM methods occasionally take azimuthal average over $\boldsymbol{k}$ values that share the same radius from the center. In this research, we use azimuthal average of $g_{one}(\boldsymbol{k}, t)$ to compare with TTCF. We use $\langle \cdots \rangle_{\phi}$ for ensemble average over pixels ϕ whose $|\boldsymbol{k}|$ are in a certain spatial frequency range (or azimuthal average), $\overline{\cdots}$ for time averages. For

simplicity, assuming that the difference between $\sum_{i=1}^{N-j} I(\boldsymbol{k}, t_i)$ and $\sum_{i=1}^{N-j} I\left(\boldsymbol{k}, t_{i+j}\right)$ is small, after averaging over the azimuthal direction, equation 1 can be modified to

$$g_{one}(k, j\Delta t) = \langle \frac{(N-j)\sum_{i=1}^{N-j} I(\boldsymbol{k}, t_i) I\left(\boldsymbol{k}, t_{i+j}\right)}{\left[\sum_{i=1}^{N-j} I(\boldsymbol{k}, t_i)\right]\left[\sum_{i=1}^{N-j} I(\boldsymbol{k}, t_i)\right]} \rangle_{\phi}$$

$$= \frac{(N-j)(N-j)\,\langle \overline{I(\boldsymbol{k}, t_\iota) I\left(\boldsymbol{k}, t_{\iota+J}\right)} \rangle_{\phi}}{(N-j)(N-j)\langle \overline{I(\boldsymbol{k}, t_\iota)}\;\overline{I(\boldsymbol{k}, t_\iota)} \rangle_{\phi}}$$

$$= \frac{\langle \overline{I(\boldsymbol{k}, t_\iota) I\left(\boldsymbol{k}, t_{\iota+J}\right)} \rangle_{\phi}}{\langle \overline{I(\boldsymbol{k}, t_\iota)}^2 \rangle_{\phi}}. \quad (2)$$

Conversely, the TTCF assesses the temporal decay of correlation between diffraction patterns at different times. The correlation between two diffraction patterns is measured using the following equation [13].

$$G\left(k,\, t_i,\, t_{i+j}\right) = \frac{\left\langle I(\boldsymbol{k},\, t_i) I\left(\boldsymbol{k},\, t_{i+j}\right)\right\rangle_{\phi}}{\langle I(\boldsymbol{k},\, t_i)\rangle_{\phi} \left\langle I\left(\boldsymbol{k},\, t_{i+j}\right)\right\rangle_{\phi}}. \quad (3)$$

During this calculation, averaging occurs along the azimuthal direction, leading to a reduction in azimuthal resolution. By averaging over a fixed delay time $j\Delta t = t_{i+j} - t_i$, we can derive the temporal decay function g_{two}.

$$g_{two}(k,\, j\Delta t) = \overline{G\left(k,\, t_\iota,\, t_{\iota+J}\right)}. \quad (4)$$

Hereafter, when referring to both $g_{one}(k, t)$ and $g_{two}(k,\, t)$, they will be collectively denoted as $g(k, t)$. In this article, for the calculation of $g(k, t)$, the region where the length of $\boldsymbol{k}$ ranges from 3.9 to 4.1 nm^{-1} (corresponding to a thickness of one pixel) where the peak of halo pattern appeared was used. Thus, the number of pixels used for calculating $g_{one}(k, t)$ and $g_{two}(k,\, t)$ are the same. Since we are not focusing on the k dependency of $g(k, t)$, we will

omit k from hereout.

The difference between these methods becomes significant when the relaxation time is much longer than the observation time. Figure 2 depicts the dependence of $g(t)$ on the length of the observation time, as measured by OTCF and TTCF. These $g(t)$ values are derived from the same experimental data, with varying lengths of data used to calculate $g(t)$ to simulate various observation time windows. This includes using the entire time domain, as well as only half, one-third, and one-quarter of the acquired time domain. It is evident that the $g_{one}(t)$ measured by OTCF is strongly influenced by the length of the observation time. $g_{one}(t)$ decays faster with shorter observation times. Conversely, this effect is not observed in $g_{two}(t)$ measured by TTCF. Irrespective of the observation time's length, it exhibits the same time dependence.

[Figure 2 here]

This difference arises from the calculation methods of OTCF and TTCF. If we define the $\overline{I(t_\iota)}$ as I_{ave} and the deviation from the average as $\delta I(t_i)$, equation 2 can be modified to

$$g_{one}(j\Delta t) = \frac{\overline{\langle \left(I_{ave} + \delta I(t_\iota)\right)\left(I_{ave} + \delta I\left(t_{\iota+J}\right)\right)\rangle_\phi}}{\langle I_{ave}^2 \rangle_\phi} = 1 + \frac{\overline{\langle \delta I(t_\iota)\delta I\left(t_{\iota+J}\right)\rangle_\phi}}{\langle I_{ave}^2 \rangle_\phi} . \quad (5)$$

Here, due to the property of average, $\overline{\delta I(t_\iota)}$ become 0. Given that $\delta I(t_i)$ represents the deviation from the temporal average, $\delta I(t_i)$ and $\overline{\delta I(t_\iota)\delta I\left(t_{\iota+J}\right)}$ must exhibit negative values

at certain t_i and j, except when all $\delta I(t_i) = 0$. (Detailed discussion is provided in the supplemental and fig. S5.) This result demonstrates that, irrespective of the actual change of the atomic structure, $g_{one}(t) - 1$ can take negative values in the observation time. This discussion is conducted under general conditions without imposing constraints on the $\delta I(t_i)$ (except not all $\delta I(t_i) = 0$). In reality, however, $\delta I(t_i)$ often exhibits temporal correlations, with closer time intervals yield more similar values. Such behavior is particularly common for atomic structural changes and the corresponding variations in diffraction patterns. In these cases, the g_{one} typically decays gradually, beginning at time shorter than the $j\Delta t$. As a result, this $j\Delta t$ often becomes the effective upper limit of relaxation times that can be reliably measured within the length of observation time. Consequently, $g_{one}(t)$ is significantly influenced by the length of the observation time, decaying faster when the observation time is shorter. This poses challenges in measuring relaxation times longer than the observation time, as $g_{one}(t)$ is compelled to converge to 1 within the observation time. In practice, accurately measurable relaxation times are typically smaller than 1/20 or 1/400 of the observation time [5,14].

In contrast, the TTCF directly measures the correlation between two diffraction patterns through equation (3). When calculating $g_{two}(t)$ using equation (3), the length of the observation time primarily affects the number of $G(k, t_i, t_{i+j})$ for averaging to calculate $g_{two}(t)$ rather than significantly altering the shape of $g_{two}(t)$. Thus, the TTCF method is

minimally impacted by the length of observation time and does not artificially converge to 1. This characteristic suggests that TTCF can potentially measure relaxation times longer than the observation time and capture dynamics that do not converge to 1, i.e., dynamics that do not completely eliminate the correlation of diffraction patterns.

Accuracy of measurement of relaxation time and γ

In this section, we investigate the impact of varying observation times on the accuracy of fitting by simulation. In the previous section, it was suggested that the TTCF method could potentially measure relaxation times longer than the observation time through $g_{two}(t)$. However, there should be a limitation regarding the ratio between relaxation time and observation time for accurately measuring relaxation time. This limitation arises because when the relaxation time significantly exceeds the observation time, only the initial decay of $g_{two}(t)$ is observable, leading to reduced robustness against noise and decreased fitting accuracy. Here, we specifically examine how the reliability of the measured relaxation time depends on this time ratio. We utilized the following KWW equation with background intensity for fitting, as TTCF has the potential to capture dynamics that do not converge to 1.

$$\frac{(g_{two}(t)-1)}{\beta} = (1-bg)\times \exp\left(-2\left(\frac{t}{\tau}\right)^{\gamma}\right) + bg \quad (6)$$

Here, β represents the normalization factor, τ represents the relaxation time, γ represents the stretching factor, and bg represents the background. Figure 3 illustrates examples of equation

185 (6) for various values of τ, γ, and bg. $(g_{two}(t)-1)/\beta$ shifts in the time direction with
186 changes in τ. While altering only γ still passes through the same points, the point is the
187 relaxation time, and as γ increases, the change around the relaxation time becomes steeper.
188 The larger the background, the smaller the temporal change of $(g_{two}(t)-1)/\beta$.
189 Next, we evaluated the accuracy of fitting using equation (6) with various values of the
190 observation time window, τ, γ, and bg. The absolute values of the relaxation and observation
191 times are not critical; instead, the ratio between them is crucial. Therefore, we utilize the ratio
192 between them (observation time/relaxation time (R)). (If the number of time steps for
193 measurement is the same, fitting under the condition of relaxation time 1000 s and observation
194 time 500 s is identical to fitting under the condition of relaxation time 10 s and observation
195 time 5 s). It is worth noting that in this simulation, since the observation time is assumed to be
196 constant, the meaning of measuring or selecting R and τ is nearly equivalent.
197 [Figure 3 here]
198 The fitting ranges for R (τ), γ, and bg were set to 0–1000, 0.01–3, and 0–1, respectively.
199 Accuracy and precision were evaluated through four steps: Step 1 involved selecting values of
200 R, γ, and bg, and calculating $g_{two}(t)$ using equation (6) for t consisting of 500 evenly
201 spaced values on a linear scale from 0 to R. Step 2 introduced noise following a normal
202 distribution with a mean of 0 and a standard deviation of 0.02 to $g_{two}(t)$ at each t. This
203 normal distribution is identical to the distribution observed in experiments with a dose of 11.5

pA. It is worth noting that the noise becomes larger at larger t in the experiment because the number of $G(k, t_i, t_{i+j})$ used for calculating $g_{two}(t)$ become fewer at larger t. Such effect is not included in this noise. Thus, added noise is a simplified model. Step 3 entailed fitting $g_{two}(t)$ with equation (6) to obtain R, γ and bg. Steps 1–3 were repeated 50 times, and the averages and standard deviations of the measured values were calculated. The averages of obtained R, γ, and bg were used to calculate the differences from the selected values, indicating accuracy, while the standard deviation reflected precision. Step 4 encompassed repeating steps 1–3 for R ranging from 0.01 to 100, γ ranging from 0.2 to 3, and bg ranging from 0 to 1. In the Supplementary Fig. S6, the effect of noise amplitude and the number of steps is also examined using the same procedure.

The results are depicted in Figure 4. Generally, as R decreases and the background value increases, both the accuracy and precision of τ, γ, and bg diminish. A smaller R means that only the early stage of the temporal decay of $g_{two}(t)$ is observed, resulting in lower accuracy and precision. A larger background leads to a smaller temporal decay of $g_{two}(t)$, reducing robustness against noise and resulting in low accuracy and precision. With a background value of 1, no temporal decay occurs, so it is natural that the value cannot be accurately estimated.

[Figure 4 here]

We then focused on the difference caused by the γ value. There is a common trend in accuracy and precision for R, γ, and bg, except for R with γ less than 0.5. As γ decreases,

even with a small R, the accuracy and precision improve. This is because, as shown in Figure 3(b), when γ is small, a temporal decay of $g_{two}(t)$ can be observed even at small t, leading to better accuracy and precision even with a short measurement time (small R). However, for R with γ less than 0.5, as γ decreases, the accuracy and precision of R worsen. This could be because when γ becomes extremely small, as shown in Figure 3(b), the temporal decay of $g_{two}(t)$ progresses rapidly within a few time steps, making it challenging to accurately measure the relaxation time via fitting. Roughly speaking, if the ratio between observation and relaxation times is above 0.3 and the background is below 0.9, measurements can be made with an error of less than 10%. The required observation time for accurate measurement using TTCF is at least 60 times smaller compared to OTCF. This advantage is well-suited for studying the glass transition phenomenon where relaxation times vary rapidly near the glass transition temperature, allowing for measurement across wider temperature ranges.

Here, we outline the advantages and disadvantages of OTCF and TTCF. OTCF can measure relaxation time without averaging over the azimuthal direction in the diffraction pattern, providing resolution in the azimuthal direction [9]. Therefore, OTCF has the potential to uncover azimuthal dependencies of relaxation time. Indeed, radius dependence on relaxation time has already been reported [15,16], and a possibility exists that relaxation time also depends on the azimuthal angle. On the other hand, although the TTCF method loses resolution along the azimuthal direction, it can measure longer relaxation times relative to the observation time.

This advantage is suitable for measuring slow dynamics observed in glass at low temperature.

Sensitivity analysis

In the previous section, we explored how the length of observation time affects measurement accuracy by assessing the error caused by noise. Here, we verify the extent of reliability of the obtained results through sensitivity analysis. Sensitivity analysis is a method for quantifying the extent to which variations in input parameters influence the corresponding changes in output parameters. In this study, we introduce noise into the experimental 5D-STEM data and examine the robustness of the fitting results against this noise to evaluate the reliability of extracted quantities, such as the relaxation time. This analysis used the experimental 5D-STEM data with an 11.5 pA dose. The measured distributions of relaxation time, γ, and background from the data before adding noise are displayed in Figure 5 (a)–(c). When comparing the distribution of relaxation times and background, we observed mainly two types of combinations: short relaxation time with high background and long relaxation time with low background. Large γ are observed with small background and relaxation time of 10^3~10^4 (pair plot shown in Figure S2).

[Figure 5 here]

$(g_{two}(t) - 1)/\beta$ calculated from the experimental 5D-STEM data contains noise of a normal distribution with a mean of 0 and a standard deviation of 0.02. We generated noise from

261 the same normal distribution, readded it to the experimental 5D-STEM data, and fitted it with
262 the modified KWW function with background (equation (6)) 50 times, measuring averages and
263 standard deviation. To quantify the spread in the measured values against the average value,
264 we evaluate the dispersion of the relaxation time—whose range is relatively large—using its
265 coefficient of variation (C. V.; standard deviation/average), whereas the smaller-range
266 parameters γ and background are assessed by their respective standard deviations. Large C.
267 V. or standard deviation values suggest that the measured results are significantly affected by
268 noise, indicating lower reliability of those measured values.
269 The distributions of the C. V. and standard deviations are shown in Figure 5(d)–(f), with
270 relative frequencies and cumulative relative frequencies displayed in Figure 5(g)–(i). Over 70%
271 of points have a C. V. of relaxation times smaller than 0.1. Regarding γ and background, over
272 80% of points have standard deviations for γ and background smaller than 0.05. This
273 indicates that measurements for over 70% of points have errors with a C. V. of less than 10%
274 for the relaxation time and errors with a standard deviation of less than 0.05 for γ and
275 background, for over 80% of points. Thus, most points are robust against noise.
276 To validate points with low precision, we created pair plots of measured values against C. V.
277 or standard deviations (Detailed pair plots are shown in Fig. S7). The results are displayed in
278 Figure 6. As shown in the upper right panel in Fig. 6, the precision of combinations involving
279 short relaxation time with high background and long relaxation time with low background are

high. These combinations of values are situated in the small standard deviation (high precision) areas in Figure 4 (upper left and bottom right areas of each figure in Figure 4).

[Figure 6 here]

As illustrated in the top row in Fig. 6, C. V. increases with long relaxation time, small γ, and medium backgrounds. This occurs because, when γ is small, the change in $g_{two}(t)$ towards the end of relaxation becomes more gradual, making it challenging to distinguish background noise from the late stage of prolonged and gradual relaxation. For similar reasons, the standard deviations in background values are also large, particularly when relaxation times are long and γ is small (shown in the right bottom panel in Fig. 6). However, the standard deviations of γ do not exhibit any clear correlation between relaxation time, γ, and background. If anything, the standard deviation of γ increases when the background has larger values. These points where the measurement precision deteriorates correspond to the upper right area of each panel in Figure 4, aligning with the results in the previous section.

Additionally, as depicted in the top right panel in Fig. 6, the length of relaxation time where the assumed precision of relaxation time begins to degrade is also around 3000 s. This value is approximately three times the observation time(1115.6 s) and corresponds to R = 0.3, in agreement with the results presented in the previous section.

Based on these results, it is feasible to estimate the measurable relaxation time from the size of the noise and the observation time. Furthermore, it is advisable to conduct a sensitivity

299 analysis to assess actual reliability.

300

301 **Beam irradiation effect**

302 Finally, we investigated the effect of beam irradiation on TTCF relaxation measurements, an
303 aspect that has not been thoroughly evaluated to date. Electron beam irradiation may potentially
304 reduce the relaxation time by modifying the sample structure [11,17,18], a phenomenon known as
305 beam damage. Beam damage encompasses thermal effects, ionization, charge up, and knock-
306 on damage [19]. It is already known that irradiation increases the sample temperature by only a
307 few millikelvins and does not impact the relaxation time of metallic glass [4,10]. Ionization and
308 charge up primarily affect insulating samples; metallic glass, being a conductor, is less affected.
309 Knock-on is displacement caused by the electron irradiation, could be the most significant in
310 our experiment. This type of damage occurs when the acceleration voltage surpasses a
311 threshold voltage, depending on atomic structures. The threshold voltage varies with atomic
312 species, surrounding atoms, irradiation direction, and temperature. Estimating knock-on
313 damage, especially in glass materials lacking periodic atomic structures, proves challenging.

314 [Figure 7 here]

315 To gauge the irradiation effect, we replicated the experiment with varying doses. Figure 7
316 displays the positional average of the $g_{two}(t)$ function measured by the TTCF at different
317 doses of 11.5, 5.8, and 2.8 pA. The time dependencies of $g_{two}(t)$ were consistent across all

318 dose levels, with no noticeable acceleration of relaxation with increasing dose. This could be
319 due to the limited effective dose amount. In this method, the electron beam scans, and the
320 irradiation time per position is quite brief. The electron counts per scan are 9500, 4800, and
321 2300 e^- at 11.5, 5.8, and 2.8 pA electron beams, respectively. Scanning occurs approximately
322 every 1.9 s, resulting in a net irradiation rate of 5000, 2500, 1200 e^-/s at 11.5, 5.8, and 2.8 pA
323 electron beams, respectively. Figure 8 showcases the spatial distributions and histograms of
324 relaxation time, γ, and background at each dose rate. Although the observation areas were not
325 perfectly identical, we compared the histograms of relaxation time, γ, and background. The
326 fitting ranges for relaxation time, γ, and background were 0–5 $\times$ 10^9, 0–3, and 0–1,
327 respectively. As a reference, supplemental Fig. S8 shows the results obtained from the same
328 dataset using OTCF.
329 [Figure 8 here]
330 It is worth noting that the measured relaxation time is longer than previous research[20]. This
331 discrepancy is attributed to aging[12]. Indeed, when the relaxation time was measured promptly
332 after heating using TTCF, it showed good agreement with results obtained by other
333 measurement methods[8]. As evident in the histograms of relaxation time, γ, and background,
334 their shapes remained consistent across different doses. Since no significant differences were
335 observed among the various doses, we conclude that dose rate does not impact relaxation time
336 measurements via TTCF. This result is different from previous result which indicates that the

dose rate affects relaxation time measurements by ECM[21]. This discrepancy derives from the difference in irradiation mode and dose rate. The previous results used TEM mode and continuously irradiated electron beam. On the other hand, we used STEM mode and intermittently irradiated electron beam. This difference makes the dose rate different. The dose rate in previous research ranged from 1×10^5 to 4×10^5 $e^-/\mathrm{nm}^2/\mathrm{s}$, and our dose rate ranged from 2.5×10^3 to 1×10^4 $e^-/\mathrm{nm}^2/\mathrm{s}$. Our dose rate is extremely low compared with the previous research. Thus, we conclude that the dependence of relaxation time on dose rate was not observed in our experiment.

Conclusion

Although the measurement of relaxation times in amorphous materials using 5D-STEM still faces limitations—such as the lack of depth resolution and the inability to resolve detailed atomic-scale structural changes—it nonetheless provides a powerful approach, enabling measurements on the nanometer scale. In this study, our focus was on comparing OTCF and the TTCF for measuring relaxation time. While TTCF sacrifices azimuthal direction resolution in the diffraction pattern, it remains unaffected by the length of observation time when measuring temporal decay. Hence, the TTCF proves more adept at measuring long relaxation times. We assessed the errors in measured relaxation time, γ, and backgrounds stemming from insufficient measurement duration. Furthermore, we confirmed that varying dose amounts have

no discernible impact on the relaxation process.

Acknowledgment

We thank Ms. K. Shiomi for her help with preparation of the sample and Prof. T. Sannomiya for advice on STEM electron optics. This work was supported by JSPS KAKENHI Grant Number JP23K13076.

Reference

1. Ruta, B., Pineda, E., & Evenson, Z. (2017, November 27). Relaxation processes and physical aging in metallic glasses. *Journal of Physics Condensed Matter*. Institute of Physics Publishing.
2. Caronna, C., Chushkin, Y., Madsen, A., & Cupane, A. (2008). Dynamics of nanoparticles in a supercooled liquid. *Physical Review Letters*, *100*, 8–11.
3. Voyles, P. M., & Muller, D. A. (2002). Fluctuation microscopy in the STEM. *Ultramicroscopy*, *93*, 147–159.
4. He, L., Zhang, P., Besser, M. F., Kramer, M. J., & Voyles, P. M. (2015). Electron Correlation Microscopy: A New Technique for Studying Local Atom Dynamics Applied to a Supercooled Liquid. *Microscopy and Microanalysis*, *21*, 1026–1033.
5. Zhang, P., Maldonis, J. J., Liu, Z., Schroers, J., & Voyles, P. M. (2018). Spatially heterogeneous dynamics in a metallic glass forming liquid imaged by electron correlation microscopy. *Nature Communications*, *9*, 1129.
6. Nakazawa, K., & Mitsuishi, K. (2023). Development of temporal series 4D-STEM and application to relaxation time measurement. *Microscopy*, *72*, 446–449.
7. Kuwahara, M., Yokoi, R., Mizuno, L., Togashi, N., Yoshida, Y., Nagata, W., Furui, M., Nakakura, K., & Ishida, T. (2020). Time-resolved Transmission Electron Microscope Using Pulsed Electron Waves. *Microscopy*, *55*.
8. Nakazawa, K., Mitsuishi, K., Iakoubovskii, K., Kohara, S., & Tsuchiya, K. (2024). Structure-dynamics relation in metallic glass revealed by 5-dimensional scanning transmission electron microscopy. *NPG Asia Materials*, *16*, 57.
9. Huang, S., & Voyles, P. M. (2023). Momentum Transfer Resolved Electron Correlation

Microscopy. *Ultramicroscopy*, 113886.

10. Zhang, P., He, L., Besser, M. F., Liu, Z., Schroers, J., Kramer, M. J., & Voyles, P. M. (2017). Applications and limitations of electron correlation microscopy to study relaxation dynamics in supercooled liquids. *Ultramicroscopy*, *178*, 125–130.
11. Spangenberg, K., Hilke, S., Wilde, G., & Peterlechner, M. (2021). Direct View on Non - Equilibrium Heterogeneous Dynamics in Glassy Nanorods. *Advanced Functional Materials*, *31*, 2103742.
12. Evenson, Z., Ruta, B., Hechler, S., Stolpe, M., Pineda, E., Gallino, I., & Busch, R. (2015). X-Ray Photon Correlation Spectroscopy Reveals Intermittent Aging Dynamics in a Metallic Glass. *Physical Review Letters*, *115*, 175701.
13. Madsen, A., Leheny, R. L., Guo, H., Sprung, M., & Czakkel, O. (2010). Beyond simple exponential correlation functions and equilibrium dynamics in x-ray photon correlation spectroscopy. *New Journal of Physics*, *12*. https://doi.org/10.1088/1367-2630/12/5/055001.
14. Paeng, K., Park, H., Hoang, D. T., & Kaufman, L. J. (2015). Ideal probe single-molecule experiments reveal the intrinsic dynamic heterogeneity of a supercooled liquid. *Proceedings of the National Academy of Sciences of the United States of America*, *112*, 4952–4957.
15. Neuber, N., Gross, O., Frey, M., Bochtler, B., Kuball, A., Hechler, S., Yang, F., Pineda, E., Westermeier, F., Sprung, M., Schäfer, F., Gallino, I., Busch, R., & Ruta, B. (2022). Disentangling structural and kinetic components of the α -relaxation in supercooled metallic liquids. *Communications Physics*, *5*. https://doi.org/10.1038/s42005-022-01099-4.
16. Ruta, B., Baldi, G., Chushkin, Y., Rufflé, B., Cristofolini, L., Fontana, A., Zanatta, M., & Nazzani, F. (2014). Revealing the fast atomic motion of network glasses. *Nature Communications5, , 5*, 3939.
17. Nino, A., Nagase, T., & Umakoshi, Y. (2005). Electron Irradiation Induced Nano-Crystallization in $Fe_{77}Nd_{4.5}B_{18.5}$ Metallic Glass. *MATERIALS TRANSACTIONS*, *46*, 1814–1819.
18. Nagase, T., Nino, A., Hosokawa, T., & Umakoshi, Y. (2007). Electron Irradiation Induced Crystal-to-Amorphous-to-Crystal Transition in Some Metallic Glasses. *MATERIALS TRANSACTIONS*, *48*, 1651–1658.
19. Egerton, R. F. (2019). Radiation damage to organic and inorganic specimens in the TEM. *Micron*, *119*, 72–87.
20. Qiao, J. C., Casalini, R., & Pelletier, J. M. (2015). Main (α) relaxation and excess wing in $Zr_{50}Cu_{40}Al_{10}$bulk metallic glass investigated by mechanical spectroscopy. *Journal of Non-Crystalline Solids*, *407*, 106–109.
21. Vaerst, O., Wilde, G., & Peterlechner, M. (2023). Beam Effects on Atomic Dynamics in Metallic Glasses Studied With Electron Correlation Microscopy. *Microscopy and Microanalysis*, *29*, 1870–1878.

Figure legends

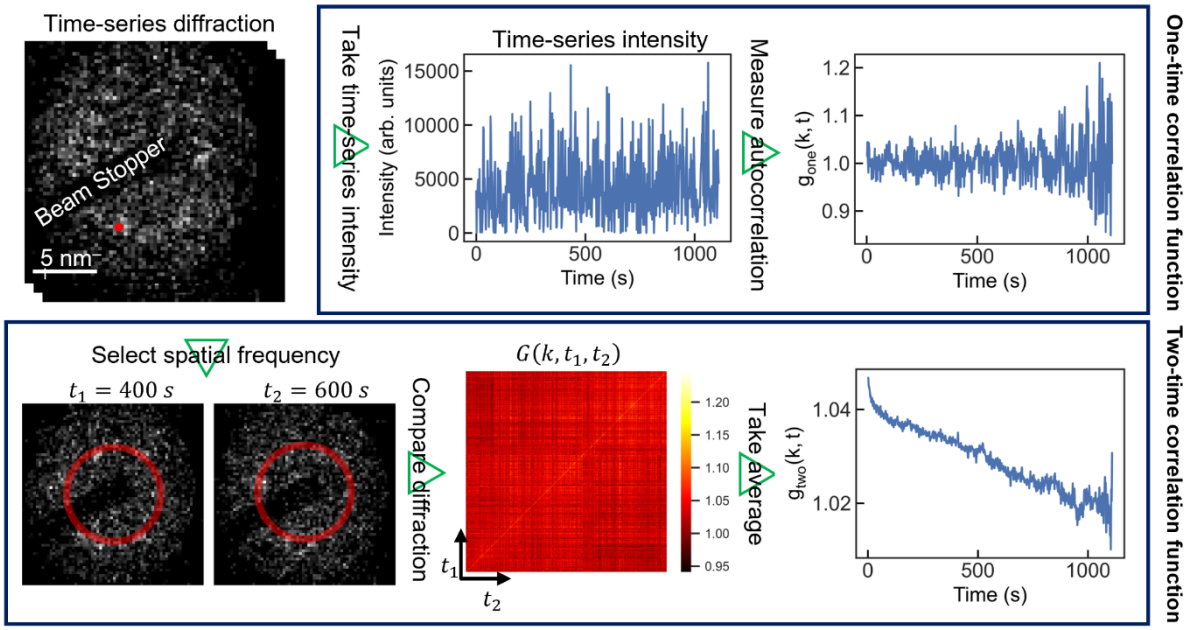


Figure 1. Schematic illustrating the processes for calculating $g(k,\ t)$ using OTCF and TTCF. Time-series intensity is extracted from the red point in the time-series diffraction patterns. $G(k,\ t_1,\ t_2)$ is determined from the red circular line depicted in the diffraction patterns at the bottom left.

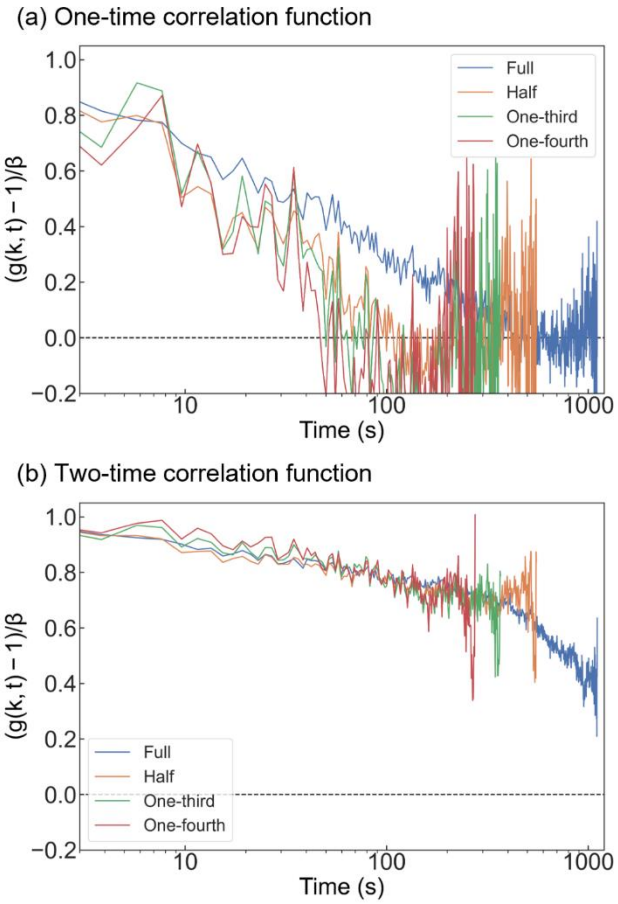
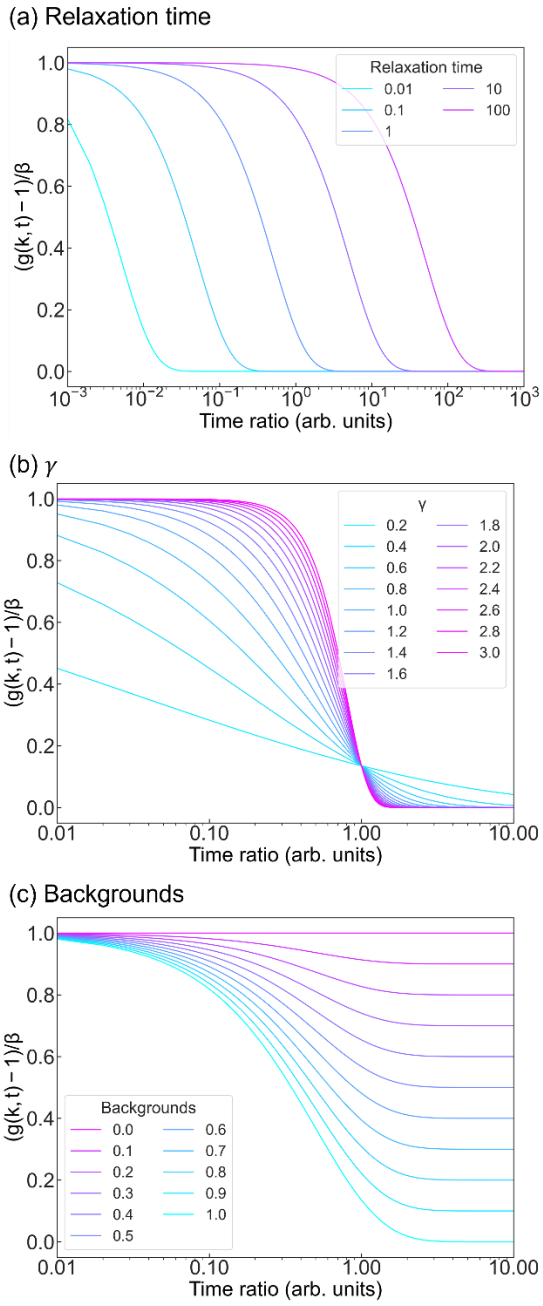


Figure 2. Comparison of relaxation curves obtained using (a) OTCF and (b) TTCF. β represents the normalization factor.



433

434 Figure 3. The dependency on (a) Relaxation time τ, (b) Stretching factor γ, and (c)

435 Background bg in equation (6). Each variable is studied independently while keeping the

436 others constant. Relaxation time was set at 1, γ at 1, and background intensity at 0.

437

438

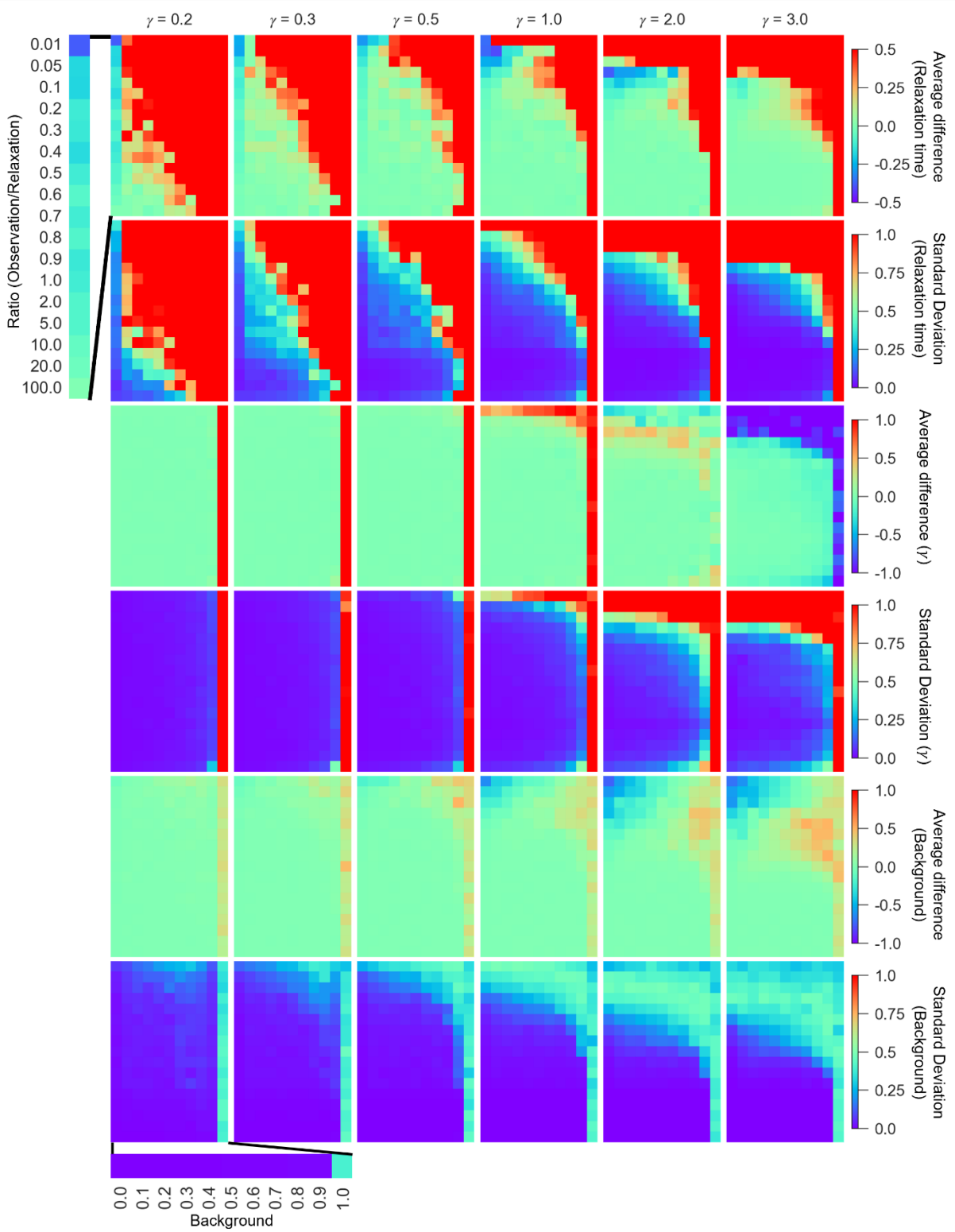
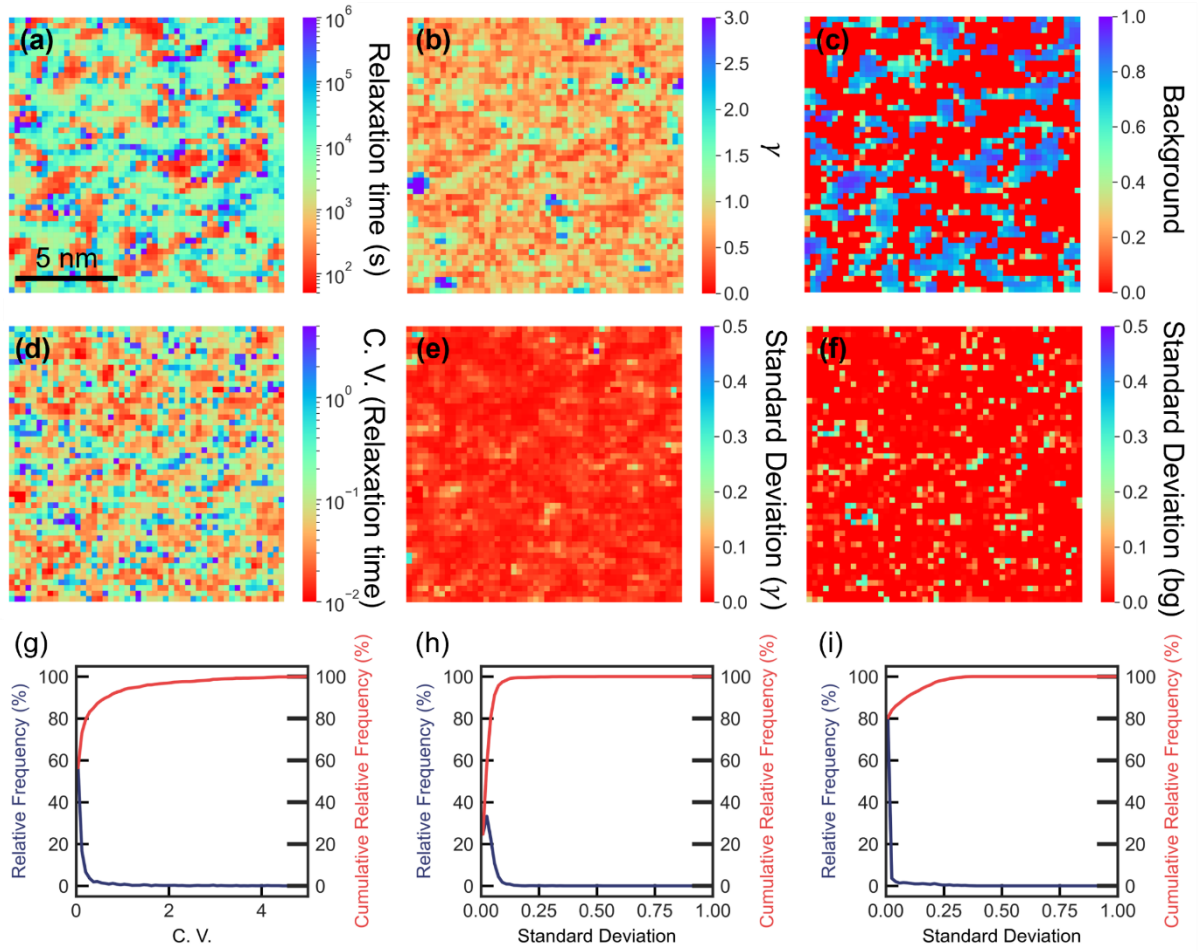


Figure 4. Average differences (accuracy) and standard deviations (precision) are shown in the 1st and 2nd rows for the ratio (Observation time/Relaxation time), in the 3rd and 4th rows for γ,

442 and in the 5^{th} and 6^{th} rows for background. These values are presented at each point along the
443 vertical axis (Observation time/Relaxation time), horizontal axis (background), and γ
444 (column). We show enlarged view of vertical axis (Observation time/Relaxation time) and
445 horizontal axis (background) at the left end and bottom of the figures. In all the figures, the
446 values on the vertical and horizontal axes are consistent.



447

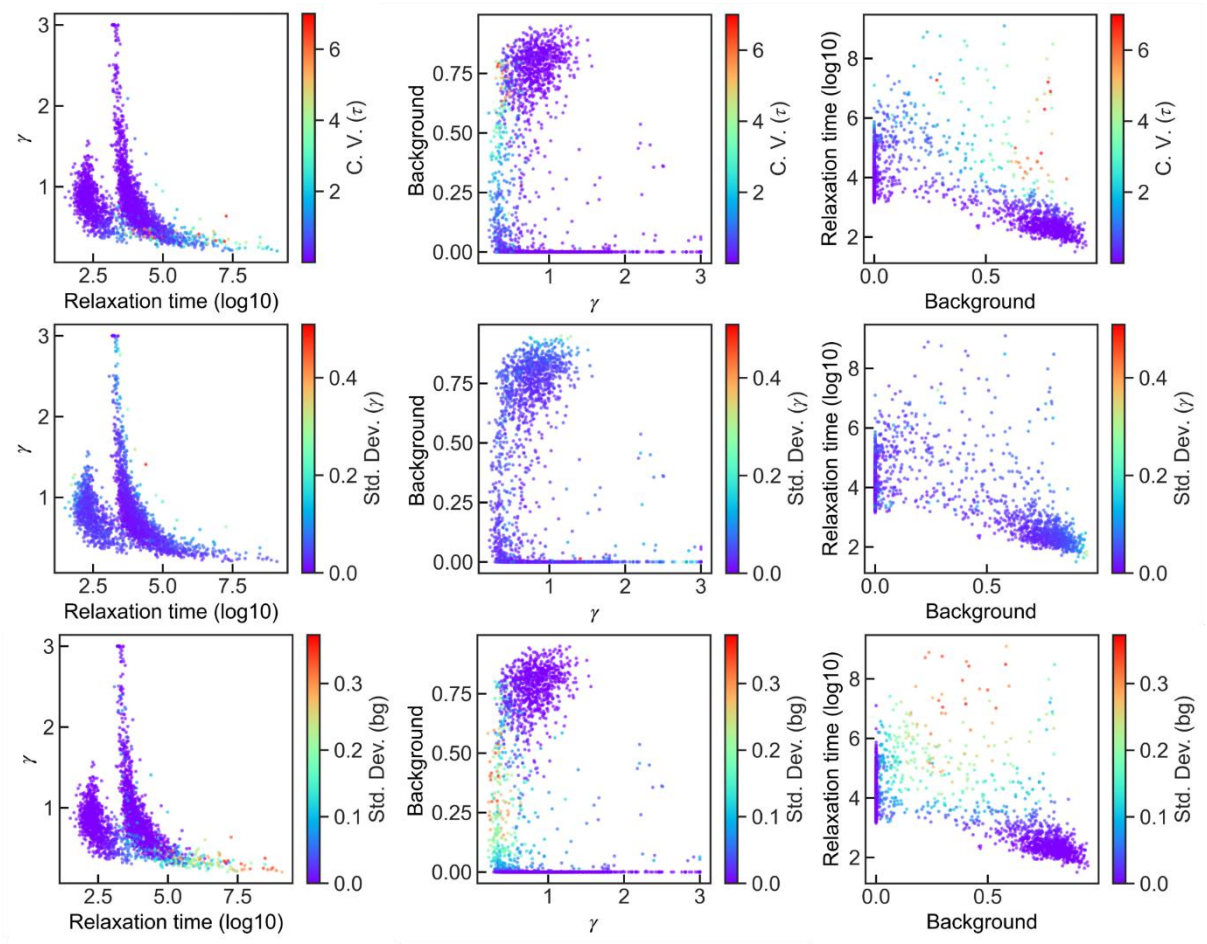
448 Figure 5. Spatial distributions of (a) relaxation time, (b) γ, (c) background, (d) C.V. of

449 relaxation time, (e) standard deviation of γ, and (f) standard deviation of background. Relative

450 frequency and cumulative relative frequency of (g) C. V. of relaxation time, (h) standard

451 deviation of γ, and (i) standard deviation of background. These data were measured

452 experimentally from $Zr_{50}Cu_{40}Al_{10}$ metallic glass.



453

454 Figure 6. The relationships among the relaxation time (τ), γ, the background (bg), the
455 coefficient of variation (C.V.) of relaxation time, and the standard deviations of γ and
456 background. Here, τ denotes the relaxation time and bg represents the background. The top
457 panels show how the C.V. (τ) varies with relaxation time, γ, and background. The middle panels
458 depict the corresponding relationship for the standard deviation of γ, while the bottom panel
459 presents it for the standard deviation of background.

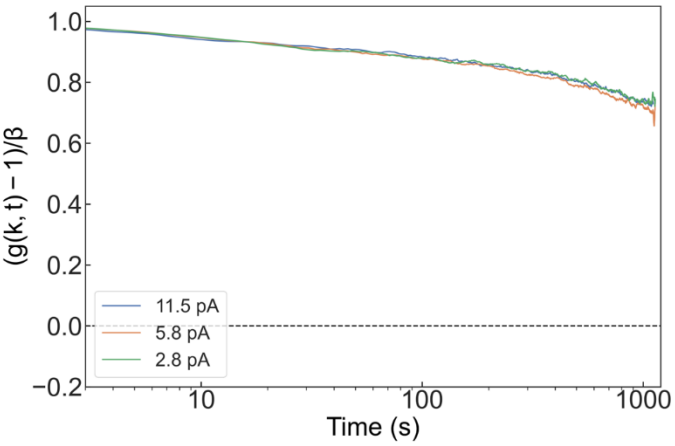
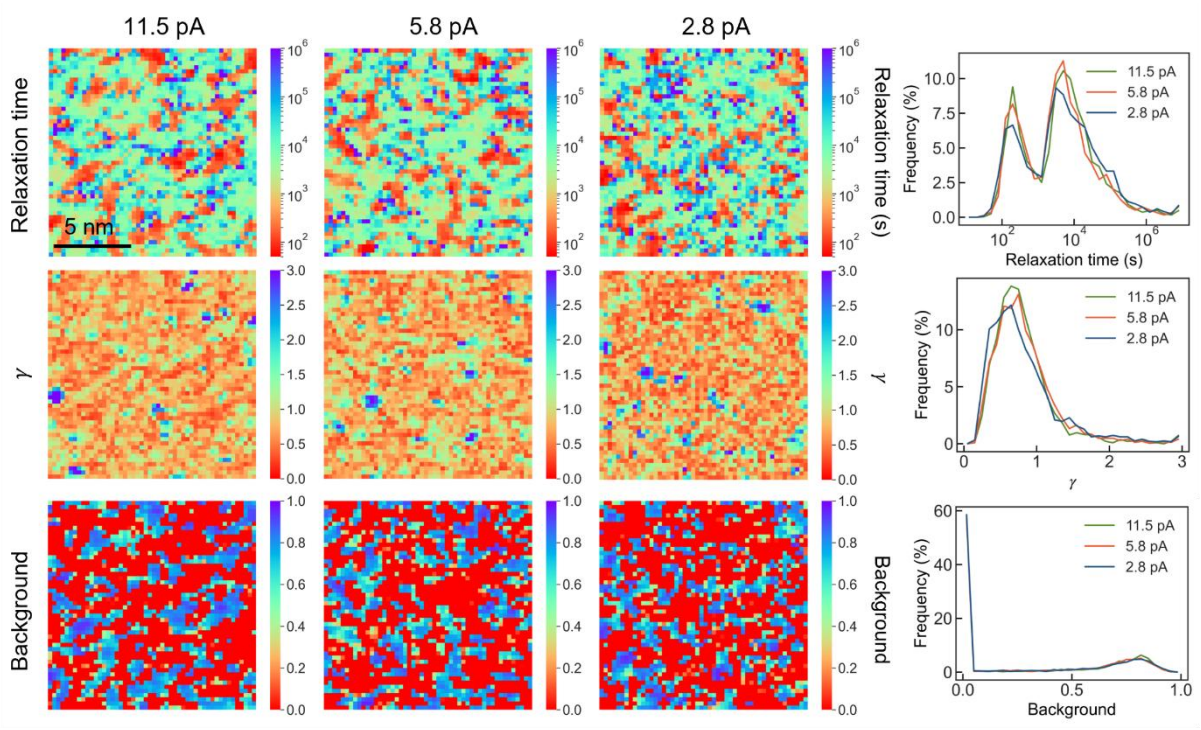


Figure 7. Positional average of $(g(k,\ t) - 1)/\beta$ for each dose amount (11.5, 5.8, and 2.8 pA).



462

463 Figure 8. Spatial distributions and histograms of relaxation time, γ, and background for each

464 dose amount. These data were measured experimentally from $Zr_{50}Cu_{40}Al_{10}$ metallic glass.

465